

Anion Charge and Lattice Volume Maps for Searching Lithium Superionic Conductors

Zhenming Xu and Hong Zhu*

Cite This: *Chem. Mater.* 2020, 32, 4618–4626

Read Online

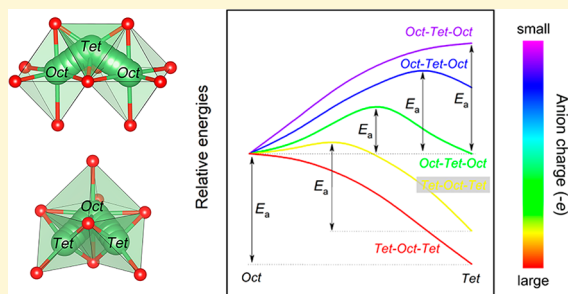
ACCESS |

Metrics & More

Article Recommendations

Supporting Information

ABSTRACT: The effects of anion charge and lattice volume (lithium–anion bond length) on lithium ion migration have been investigated by utilizing the density functional theory calculations combined with the anion sublattice models. It is found that anion charge and lattice volume have great impacts on the activation energy barrier of lithium ion migration, which is validated by some reported sulfides. For the tetrahedrally occupied lithium, the less negative the anion charge is, the lower the migration energy barrier is likely to be. While for the octahedrally occupied lithium, the more negative anion charge is, the lower migration energy barrier is. Based on the full understandings of the anion sublattice model, general design strategies for developing lithium superionic conductors were proposed. Adjusting the electronegativity difference between the anion element and the nonmobile cation element by selecting the most suitable nonmobile cation element without changing the crystal structure framework can achieve low activation energy barriers for lithium ion migration. For the desired lithium superionic conductors with tetrahedrally occupied lithium, the fine nonmobile cation elements should give preference to those elements located at the right top of the periodic table of elements with large electronegativities. For the lithium superionic conductors with octahedrally occupied lithium, the fine nonmobile cation elements should give preferences to the elements located at the left bottom of the periodic table with small electronegativities.



1. INTRODUCTION

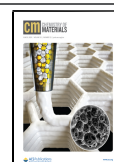
Today, lithium ion battery (LIB) techniques provide many conveniences for people's lives, powering portable electronic devices.¹ However, we are encountering safety issues when using the commercial LIBs in the application scenarios of large-scale energy storage in electric vehicles, because of the flammability of the liquid organic electrolyte.^{2,3} Fortunately, replacing the currently employed flammable organic electrolytes with the inflammable solid-state electrolyte (SSE) materials and matching with lithium metal anodes to construct all-solid-state lithium ion batteries (ASSLIBs) not only solves safety issues but also drastically promotes the energy density of LIBs,^{4–6} making electric cars run farther. Correspondingly, high lithium ionic conductivities at room temperature (10^{-3} – 10^{-2} S cm⁻¹) of SSE materials are the essential prerequisite for constructing ASSLIB systems. At present, some lithium superionic conductors, e.g., $\text{Li}_7\text{La}_3\text{Zr}_2\text{O}_{12}$,⁷ $\text{Li}_{1+x}\text{Al}_x\text{Ti}_{2-x}(\text{PO}_4)_3$,⁸ $\text{Li}_{10}\text{GeP}_2\text{S}_{12}$ (LGPS),⁹ and $\text{Li}_7\text{P}_3\text{S}_{11}$,¹⁰ have been widely studied and successfully developed as SSE materials, and the state-of-the-art ionic conductivities at room temperature of 12–17 mS cm⁻¹ are experimentally realized in $\text{Li}_{10}\text{GeP}_2\text{S}_{12}$ and $\text{Li}_7\text{P}_3\text{S}_{11}$ sulfides. To efficiently exploit more advanced lithium superionic conductors, it is quite necessary to deeply understand the fast ion migration mechanism in the state-of-the-art superionic conductors and even propose proper design strategies.

Among the various studies on understanding fast ion migration, topology analysis of the ion migration pathways is possibly the most common method.^{11–13} Eremin et al. applied the geometrical-topological approach based on the Voronoi partition theory to perform high-throughput searchings for new potential potassium solid electrolytes.^{14,15} Ceder et al. calculated the topology features of the anion sublattice structures for various lithium sulfides, revealed a fundamental relationship between the anion packing pattern and lithium ionic transport, and eventually proposed the design concept of a body-centered cubic-like anion sublattice with face-shared tetrahedral lithium sites facilitating lithium ion migration.¹¹ Subsequently, they utilized this design concept and computationally predicted a new lithium superionic conductor, $\text{Li}_2\text{Zn}_{0.5}\text{PS}_4$, with exceptionally high lithium ion conductivity at room temperature.¹⁶ In addition, Mo et al. pointed out the unique feature of the common lithium superionic conductors with abundant enlarged lithium sites caused by the large local

Received: March 6, 2020

Revised: May 14, 2020

Published: May 14, 2020



spaces (fractionally occupied lithium sites) in crystal structures and identified many new structures as the fast lithium ion conductors by the high-throughput screenings combined with this quantified feature.¹² However, these understandings based on the topology of lithium migration channel are insufficient to explain the enhanced ionic conductivity by Cl doping and isovalent cation substitution in LGPS families. The Cl-doped silicon-based $\text{Li}_{9.54}\text{Si}_{1.74}\text{P}_{1.44}\text{S}_{11.7}\text{Cl}_{0.3}$ shows a quite high ionic conductivity of 25 mS/cm at room temperature (twice that of original LGPS),¹⁷ in which thoroughly substituting Ge in LGPS with Si and partially replacing S with Cl have negligible influence on the lattice constants ($a = 8.710 \text{ \AA}$ and $c = 12.57 \text{ \AA}$ of $\text{Li}_{9.54}\text{Si}_{1.74}\text{P}_{1.44}\text{S}_{11.7}\text{Cl}_{0.3}$ ¹⁷ vs $a = 8.717 \text{ \AA}$ and $c = 12.63 \text{ \AA}$ of LGPS⁹), the local atom arrangements, and even the morphologies of lithium ion migration channel. Thus, there would be other important factors influencing lithium ion transport in addition to the topology-based structure features.

In ionic materials, the total energy landscape of Li ion in an ionic solid can be described by the classical Coulomb-Buckingham potential model,^{18,19} which can be further divided into the short-ranged Li-anion Pauli repulsive interaction, short-ranged Li-anion electrostatic attractive interaction, and long-ranged Li-cation electrostatic repulsive interaction. The resulting total energy landscapes are mainly set by the short-ranged Li-anion interactions, so lithium ion migration in an ionic compound can be approximated by lithium ion migration in an anion sublattice model.¹³ It is also noted that Li-cation repulsive interactions also contribute to the total energy landscape to some extent, and the weight of Li-cation interaction in the total energy landscape is affected by the arrangements and valence states of cation. As mentioned in some previous works, the monovalent halogen anions have weaker interactions with lithium ions than the divalent sulfur or oxygen anions.^{20,21} It is worth noting that Zeier et al. have demonstrated the influence of lattice dynamics and lattice softness on ionic transport.^{22–25} Lattice dynamics is the manifestation of the bonding interaction in materials, not the fundamental factors of determining bonding interaction. Yet, as far as we know, there is no systematical understanding of Li-anion interaction dependent lithium ion occupation and lithium ion migration in compounds with different types of anion sublattice. Thus, this study aims to fill the existing knowledge gaps regarding the effect of the Li-anion interaction on lithium ion migration in solids.

In the most crystalline lithium compounds, lithium ions occupy the tetrahedral (*Tet*) or octahedral (*Oct*) sites, forming tetrahedral or octahedral lithium-anion polyhedrons, and the anion packing modes of more than half lithium compounds could be approximately classified into the face-centered cubic (*fcc*), body-centered cubic (*bcc*), and hexagonal close-packed (*hcp*) sublattices.¹¹ The anion sublattices of LiCoO_2 , Li_2MnO_3 , $\text{Li}_4\text{Ti}_5\text{O}_{12}$, Li_2S , LiTiS_2 , and Li_3YBr_6 can be exactly matched to *fcc* types. In $\text{Li}_7\text{P}_3\text{S}_{11}$ and $\text{Li}_{10}\text{GeP}_2\text{S}_{12}$, sulfur anion sublattices can be roughly mapped to *bcc* lattices with some distortions. In $\gamma\text{-Li}_3\text{PS}_4$ and Li_4GeS_4 , sulfur anion sublattices can be closely matched to *hcp* arrays.¹¹ Our previous studies of the *fcc* anion sublattices show that anion charge and lattice volume have great impacts on the stability of lithium ion occupation and lithium ion migration.^{26–28} Considering the excellent lithium ion migration usually occurring in those sulfide-type superionic conductors with *bcc* and *hcp* sulfur anion sublattices, such as $\text{Li}_7\text{P}_3\text{S}_{11}$ and $\text{Li}_{10}\text{GeP}_2\text{S}_{12}$, in this work, we shed lights on the effects of anion charge and lattice volume dependent Li-anion

interaction on the lithium ion occupation and lithium ion migration along different pathways in the *bcc*- and *hcp*-type anion sublattices. By the depicted anion charge and lattice volume maps, we suggested some design strategies for different diffusion paths to lower the activation energy barrier for lithium ion migration in terms of anion charge control and element selection.

2. COMPUTATIONAL METHODOLOGIES

All calculations were performed by using the Vienna *Ab initio* Simulation Package (VASP) software based on the projector augmented wave (PAW) method^{29,30} in the framework of the density functional theory (DFT).^{29,30} The generalized gradient approximation (GGA)³¹ with Perdew–Burke–Ernzerhof (PBE) exchange functional³² is utilized to solve the Schrödinger's equation of the quantum states of the electron. The energy cutoff of the plane-wave is 500 eV. The convergence criteria of the energy and force are 10^{-5} eV/atom and 0.01 eV/Å, respectively. The Monkhorst–Pack method³³ with $4 \times 4 \times 4$ and $4 \times 4 \times 2$ *k*-point meshes are employed for the Brillouin zone sampling of the *bcc*- and *hcp*-type anion sublattices, respectively. The energy landscapes and activation energy barrier of lithium ion migration in anion sublattices are calculated by the nudged elastic band (NEB) method.³⁴ During NEB calculations, only one lithium ion is allowed to relax, while sulfur (oxygen) anions are fixed in their initial positions, and this approach has been also utilized by Ceder et al.¹¹ Anion charges in the anion sublattice are changed by adjusting the uniform background charges of the whole sublattice system.

3. RESULTS AND DISCUSSION

3.1. Anion Charge and Lattice Volume Dependent Lithium Ion Occupation and Migration. First, to get the reasonable ranges of anion charge and lattice volume for the following NEB calculations, the scatter distributions of anion Bader charges and lattice volumes of lithium oxides and sulfides were investigated and are shown in Figure S1, which were directly obtained from the AFLOW database without any DFT calculation.³⁵ It can be found that oxygen anion charges are mainly spread in the range of $[-0.8e, -1.7e]$, while sulfur anion charges are principally distributed in the range of $[-0.7e, -1.5e]$. Thereby, a wider anion charge range of $[-0.5e, -1.8e]$, simultaneously covering the dominating oxygen and sulfur anion charges, was considered for the following NEB calculations. The lattice volumes of oxides and sulfides are mainly spread in the ranges of $[15 \text{ \AA}^3/\text{atom}, 30 \text{ \AA}^3/\text{atom}]$ and $[30 \text{ \AA}^3/\text{atom}, 50 \text{ \AA}^3/\text{atom}]$, respectively. In addition, Bader charges of lithium cation in both lithium oxides and sulfides are dominantly located in the range of $[+0.84e \sim +0.92e]$ (Figure S2), which are far narrower than those of anions. It indicates that the lithium ion charges in different compounds do not change a lot and thereby can be regarded as a constant.

Then, two artificial *bcc*- and *hcp*-type anion sublattices with a single lithium cation and 16 anions were built to investigate lithium ion migration in them, as illustrated in Figure 1. Only two chalcogen anion elements (oxygen and sulfur) were considered for the anion sublattice models in view of the fact that the most reported lithium superionic conductors are lithium oxides and sulfides. These sulfur (oxygen) anion sublattice models can allow us directly capture the effects of Li-anion interaction between lithium cation and its adjacent anions, which fundamentally depend on anion charge and lithium-anion bond length. In this work, for the convenience of NEB energy landscape calculations, we employed the descriptor of the anion sublattice volume instead of lithium-anion bond length, which is defined as the lattice volume

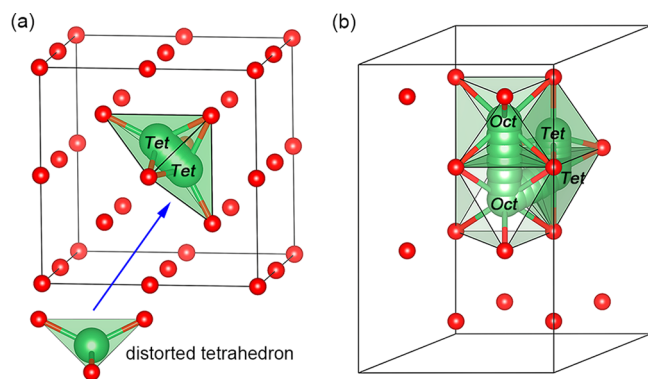


Figure 1. Structural models of (a) lithium ion migration along the *Tet*–*Tet* pathway (two adjacent tetrahedral sites) in the *bcc*-type anion sublattice with a lithium cation and 16 anions, where the lithium–anion tetrahedrons in the *bcc*-type anion sublattice are distorted with a *csm* (continuous symmetry measure) value of 2.29 (a *csm* value of 0 corresponds to a perfect tetrahedron), and (b) lithium ion migration along *Tet*–*Tet*, *Oct*–*Oct* (octahedral site to octahedral site), and *Oct*–*Tet* pathways in the *hcp*-type anion sublattice with a lithium cation and 16 anions. Anions are colored red, and lithium ions are colored green, respectively.

divided by the number of anion atoms. There is only one kind of tetrahedral interstitial site in the *bcc*-type anion sublattice (Figure 1a), corresponding to the *Tet*–*Tet* lithium ion migration pathways, and this direct lithium ion hopping between two adjacent *Tet* sites has been reported to possess the lowest activation barrier and the highest lithium ionic conductivity.¹¹ For the *hcp*-type anion sublattice model, there are two different kinds of interstitial sites, including tetrahedral and octahedral interstitial sites (Figure 1b). Thus, the occupied lithium ion in the *hcp* anion sublattice could migrate along three different direct pathways, including the *Tet*–*Tet*, *Oct*–*Oct*, and *Oct*–*Tet* pathways, and *Oct*–*Tet* is the half of *Tet*–*Oct*–*Tet* and *Oct*–*Tet*–*Oct* pathways.

3.1.1. *bcc*-Type Anion Sublattices. Then, we performed NEB calculations to get the energy landscapes of lithium ion migration in the *bcc*-type sulfur (oxygen) anion sublattices with respect to anion charge and lattice volume. Lithium ion migration between two face-shared distorted lithium–anion tetrahedral sites (namely, the *Tet*–*Tet* pathway) in the *bcc*-type anion sublattice passes through a distorted triangular anion bottleneck (Figure 1a), whose relative energy with respect to the initial *Tet* site is the activation energy barrier (E_a) of lithium ion migration along this way. Note, achieving high ionic diffusivity not only needs small E_a , but also claims a large prefactor. Considering the most contribution of small E_a to high ionic diffusivity and the complex composition of the prefactor, in this work we mainly focused on anion charge and lattice volume dependent E_a for lithium ion diffusion. The NEB calculated E_a values of lithium ion migration in the *bcc*-type sulfur and oxygen anion sublattices are shown in Figures 2 and S3, respectively. To clearly show E_a variations with respect to different anion charges at any constant lattice volume, those heatmaps of Figures 2 and S3 are transformed into the facetgrid plots, as illustrated in Figures S5 and S6, respectively. It can be clearly seen that the anion charge and lattice volume show similar influences on E_a for both sulfur and oxygen anion sublattices. E_a variation ranging from 0 to 0.42 eV in the whole anion charge and lattice volume space of the *bcc*-type oxygen anion sublattice (Figure S3) is much narrower than that of the

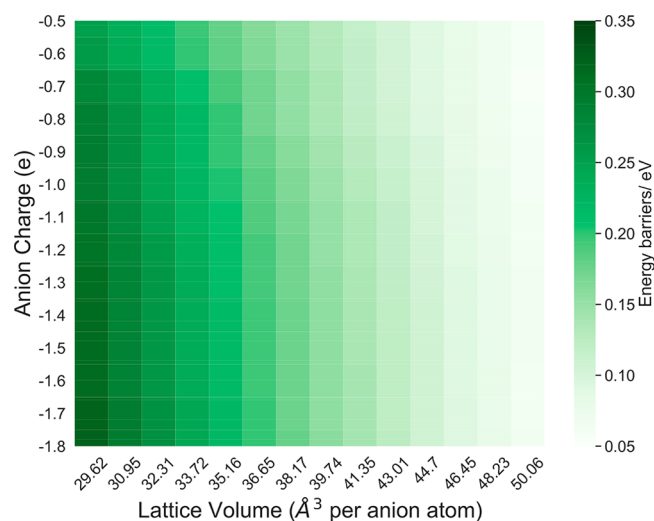


Figure 2. Heat maps of the calculated E_a of lithium ion migration in the *bcc*-type sulfur anion sublattices along the *Tet*–*Tet* migration pathway with respect to anion charge and lattice volume. The corresponding data are also shown as a matrix table in Table S4.

fcc-type oxygen anion sublattice from 0.25 to 1.5 eV (Figure S4a). In addition, the maximum variations of E_a with respect to different anion charges at any constant lattice volume are ~ 0.12 and 0.07 eV, respectively, for the oxygen and sulfur anion sublattices (Figures S5 and S6). They consistently indicate that E_a values of lithium ion migration in the *bcc*-type anion sublattices are not only smaller, but also less sensitive to the variations of anion charge than that in the *fcc*-type anion sublattice. It is worth noting that lithium compounds possessing the *bcc*-type anion sublattices are much fewer than those with the *fcc*- and *hcp*-type anion sublattices (Table S1), although they usually show higher lithium ion conductivities.¹¹ Overall, anion charge and lattice volume (lithium–anion bond length) dependent Li–anion interactions have smaller impacts on E_a of lithium ion migration along the *Tet*–*Tet* pathways in the *bcc*-type anion sublattices. From the energy maps, the most important conclusion which can be made is that the activation energy depends more strongly on lattice volume than anion charge.

In the whole anion charge and lattice volume space, the more negative anion charges can lead to slightly higher E_a for lithium ion migration in the *bcc*-type anion sublattice along the *Tet*–*Tet* pathways at any constant lattice volume (Figures S5 and S6), and the large lattice volumes can reduce E_a at any constant anion charge (Figures 2 and S3). In short, the small negative anion charges and large lattice volumes can lead to lower E_a . Therefore, the small negative anion charges and large lattice volumes (lithium–anion bond lengths) are essential for achieving fast lithium ion migration in lithium compounds with the *bcc*-type anion sublattices. It is worth noting that these variation trends of E_a with respect to the anion charge and lattice volume are much more interesting than the absolute values of E_a . These observed trends are also found in the previous experimental results for some sulfide-type lithium conductors with the *bcc*-type anion sublattices. The higher element electronegativity of Ge^{4+} vs Sn^{4+} (2.116 vs 1.877)³⁶ lead to fewer negative sulfur anion charges in $\text{Li}_{10}\text{GeP}_2\text{S}_{12}$ ($-0.151e$ vs $-0.168e$ in $\text{Li}_{10}\text{SnP}_2\text{S}_{12}$, Hirshfeld charge),²⁷ and the Li–S average bond length of $\text{Li}_{10}\text{GeP}_2\text{S}_{12}$ is 2.585 \AA , slightly larger than 2.578 \AA of $\text{Li}_{10}\text{SnP}_2\text{S}_{12}$.²⁷ The relatively

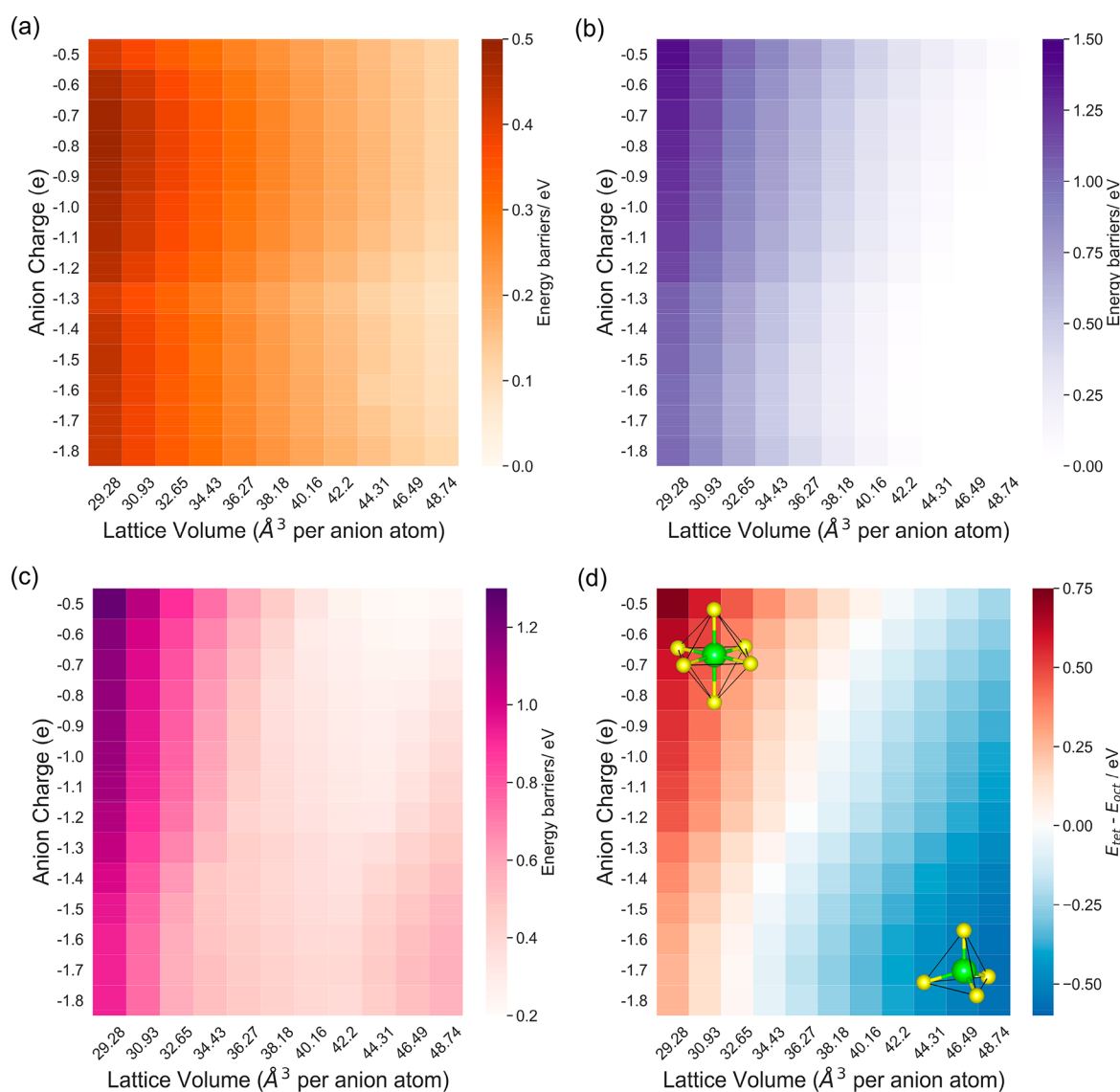


Figure 3. Heat maps of the calculated E_a values of lithium ion migration in the *hcp*-type sulfur anion sublattices along the (a) *Tet*–*Tet*, (b) *Oct*–*Oct*, and (c) *Oct*–*Tet* (*Tet*–*Oct*) migration pathways with respect to anion charge and lattice volume and (d) energy differences of the occupied lithium between the *Tet* site and the *Oct* site in the *hcp*-type sulfur anion sublattices with respect to anion charge and lattice volume. The corresponding data in heat maps are also shown as a matrix table in Tables S5–S8.

lower negative sulfur anion charge together with the slightly larger bottleneck area eventually leads to relatively lower E_a of $\text{Li}_{10}\text{GeP}_2\text{S}_{12}$ compared to that of $\text{Li}_{10}\text{SnP}_2\text{S}_{12}$.^{37,38} The enhanced ionic conductivities can also be obtained by the monovalent Cl element doping in lithium sulfides; Cl-doped $\text{Li}_{9.54}\text{Si}_{1.74}\text{P}_{1.44}\text{S}_{11.7}\text{Cl}_{0.3}$ shows a quite higher ionic conductivity of 25 mS/cm at room temperature than LGPS,¹⁷ in which thoroughly substituting Ge of LGPS with Si and partially replacing S with Cl has negligible influence on lattice constants and even the morphologies of the lithium ion migration channel. These consistent variation tendencies of E_a in the cation-substituted $\text{Li}_{10}\text{MP}_2\text{S}_{12}$ (where M = Ge and Sn) and chlorine-doped $\text{Li}_{9.54}\text{Si}_{1.74}\text{P}_{1.44}\text{S}_{11.7}\text{Cl}_{0.3}$ materials are fully consistent with our findings, validating the reasonability of the *bcc*-type anion sublattice model and the corresponding analyses of Li–anion interactions.

3.1.2. *hcp*-Type Anion Sublattices. Different from the less common *bcc*-type anion sublattices, there are both tetrahedral and octahedral interstitial sites in the *hcp*-type anion sublattice

model (Figure 1b). Therefore, the discussions about lithium ion migration in the *hcp*-type anion sublattice are organized based on three different pathways, including *Tet*–*Tet*, *Oct*–*Oct*, and *Oct*–*Tet*.

3.1.2.1. *Tet*–*Tet* Pathway. The calculated E_a of lithium ion migration in the *hcp*-type sulfur (oxygen) anion sublattices along the direct *Tet*–*Tet* pathways with respect to anion charge and lattice volume are shown in Figures 3a, S7, S8, and S9. It can be observed that E_a varies from 0 to 0.5 eV in the whole anion charge and lattice volume space for the *Tet*–*Tet* migration pathways in the *hcp*-type sulfur (oxygen) anion sublattices (Figures 3a and S7), whose ranges are similar to that of the *Tet*–*Tet* migration in the *bcc*-type sulfur (oxygen) anion sublattices (Figures 2 and S3) (0–0.42 eV) and narrower than that of the *fcc*-type oxygen anion sublattice from 0.25 to 1.5 eV (Figure S4a). This relatively smaller variation of the *bcc*-type anion sublattice may be due to the more distorted lithium–anion tetrahedra (Figure S10) leading to more frustrated energy landscapes for lithium ion

migration.¹³ The maximum variation of E_a with respect to different anion charges at any constant lattice volume is only ~ 0.09 eV for the oxygen- and sulfur-anion sublattices (Figures S8 and S9), indicating that E_a of lithium ion migration along the *Tet*–*Tet* pathways in lithium compounds with the *hcp*-type anion sublattices are much less sensitive to anion charge, which is similar to those lithium compounds with the *bcc*-type anion sublattices.

However, different from the *bcc*-type sublattice, E_a variations with respect to different anion charges at any constant lattice volume in the *hcp*-type anion sublattice are not monotonically increasing or decreasing (Figures S8 and S9), while E_a variations are monotonic for the *Tet*–*Tet* migration pathways in the *bcc*-type anion sublattice (Figures S5 and S6). It may be because of the different local environments of lithium tetrahedral sites and the diverse triangular anion bottlenecks (transition states) in the *bcc*- and *hcp*-type anion sublattice, as shown in Figure S10. Taking the *hcp*-type sulfur anion sublattice as an example (Figures 3a and S9), sulfur anion charges, ranging from $-0.8e$ to $-1.3e$, can significantly decrease E_a , while E_a gradually increases when the more negative sulfur anion charges are in the range of $[-1.3e, -1.8e]$. Discussing E_a variation with respect to the much more positive anion charges in the range of $[-0.5e, -0.8e]$ makes no sense due to the very low probability to get such small anion charges in lithium sulfides (Figure S1). Moreover, it is found that the large lattice volumes can cause low E_a at any constant anion charge, and the effect of lattice volume on E_a is larger than that of anion charge for the *Tet*–*Tet* lithium ion migration. Thus, the moderate sulfur (oxygen) anion charges near $-1.3e$ and especially large lattice volumes are beneficial to fast lithium ion migration along the *Tet*–*Tet* migration pathways in lithium compounds with the *hcp*-type sulfur (oxygen) anion sublattices, although the effects of Li–anion interaction depending on anion charge and lattice volume on the *Tet*–*Tet* lithium ion migration are limited.

3.1.2.2. Oct–Oct Pathway. Now we focus on another direct lithium ion migration pathway in the *hcp*-type anion sublattices, namely, *Oct*–*Oct* pathway. The calculated E_a values of lithium ion migration in the *hcp*-type sulfur (oxygen) anion sublattices along the *Oct*–*Oct* migration pathways with respect to anion charge and lattice volume are shown in Figures 3b, S11, S12, and S13. It can be found that E_a variation ranging from 0 to 1.5 eV in the whole anion charge and lattice volume space for the *Oct*–*Oct* migration pathways in the *hcp*-type sulfur (oxygen) anion sublattice is much wider than 0 to 0.5 eV of *Tet*–*Tet* migration pathways in both *bcc*- and *hcp*-type sulfur (oxygen) anion sublattices. The maximum variation of E_a with respect to different anion charges at any constant lattice volume is ~ 0.4 eV for the oxygen and sulfur anion sublattices (Figures S12 and S13), demonstrating that E_a of lithium ion migration along the *Oct*–*Oct* pathways in lithium compounds with the *hcp*-type anion sublattices is sensitive to the variations of anion charge and much different from the anion charge immunized *Tet*–*Tet* migration pathways. Interestingly, E_a variations with respect to anion charge and lattice volume are monotonic. In the whole anion charge and lattice volume space, the more negative anion charges can reduce E_a of lithium ion migration in the *hcp*-type anion sublattice along the *Oct*–*Oct* pathways at any constant lattice volume (Figures S12 and S13), and the large lattice volumes can make low E_a at any constant anion charge. Overall, the Li–anion interactions depending on anion charge and lattice

volume have great influences on E_a of lithium ion migration along the *Oct*–*Oct* pathways in the *hcp*-type anion sublattices, and the more negative anion charges and large lattice volumes (lithium–anion bond lengths) are essential for achieving fast lithium ion migration along the *Oct*–*Oct* pathways in lithium compounds with the *hcp*-type anion sublattices.

3.1.2.3. Oct–Tet Pathway. Lastly, we discuss the *Oct*–*Tet* pathway for lithium ion migration in the *hcp*-type anion sublattices, and it is a half of the *Tet*–*Oct*–*Tet* or *Oct*–*Tet*–*Oct* pathways, which are the most common lithium ion migration pathways in those lithium sulfides with the *hcp*-type sulfur anion sublattices.^{39–41} The calculated E_a of lithium ion migration along the *Oct*–*Tet* migration pathways and the energy differences of lithium occupation between the *Tet* and the *Oct* sites ($E_{Tet-Oct}$) in *hcp*-type sulfur (oxygen) anion sublattices with respect to anion charge and lattice volume are shown in Figures 3c,d, S14, S15, and S16. It can be observed that E_a variation ranging from 0.2 to 1.4 eV and $E_{Tet-Oct}$ variation from -0.76 to 0.9 eV in the whole anion charge and lattice volume space for the *Oct*–*Tet* migration pathways in the *hcp*-type sulfur (oxygen) anion sublattices is very wide, indicating anion charge and lattice volume have significant effects on E_a and $E_{Tet-Oct}$ values for both oxygen and sulfur anion systems. For any specific lattice volume, the more negative anion charges consistently reduce $E_{Tet-Oct}$ values (Figure 3d and S14b), and stabilizing lithium–anion tetrahedra. At any constant anion charge, $E_{Tet-Oct}$ values vary from positive to negative, and the relative stabilities of lithium–anion tetrahedra gradually increase when lattice volumes get larger. The very negative anion charge and large lattice volume cause lithium to prefer to occupy *Tet* sites in the *hcp*-type anion sublattices, and a low negative anion charge and small lattice volume cause lithium to preferentially occupy *Oct* sites (Figures 3d and S14b), the same as the *fcc*-type oxygen anion sublattices (Figure S4b). For the *Tet*–*Oct*–*Tet* and *Oct*–*Tet*–*Oct* pathways, the corresponding transition state sites are *Oct* and *Tet* sites, respectively. Because of the relative energies of the lithium ion occupying at *Tet* and *Oct* sites ($E_{Tet} - E_{Oct} > 0, = 0$, and < 0) with respect to different anion charges and lattice volumes, there are competitions of the relative energy of the equilibrium site and saddle point for the *Tet*–*Oct*–*Tet* and *Oct*–*Tet*–*Oct* pathways in the *hcp*- and *fcc*-type sublattices, consequently showing the opposite effect of the anion charge on E_a for the *Tet*–*Oct*–*Tet* and *Oct*–*Tet*–*Oct* pathways and the optimum lattice volumes for minimum E_a at one fixed anion charge (Figures 3c, S4a, and S14a). No anion charge and lattice volume optimizing minimum E_a values for the *Tet*–*Tet* and *Oct*–*Oct* pathways in the *bcc*- and *hcp*-type sublattices are found, due to no energy competitions between the equilibrium sites (*Tet* or *Oct* site) and high-energy saddle points, which are fully consistent with the previous work by Ceder et al.¹¹

There are opposite E_a responses to the anion charge for the *Tet*–*Oct*–*Tet* and *Oct*–*Tet*–*Oct* pathways. Facetgrid plots in Figures S15 and S16 show anion charge dependent E_a at different lattice volumes. Taking the sulfur anion sublattice as an example, when sulfur anion lattice volumes are small, e.g., with a value of ~ 32.65 Å³/atom, the relative energies of LiS₄ are all higher than those of LiS₆ ($E_{Tet-Oct} > 0$, Figure 3d), indicating lithium is most stable at the *Oct* site and prefers to have an octahedral lithium occupation pattern with respect to a small sulfur anion lattice volume, which is consistent with those *hcp*-type lithium sulfides with relative small lattice

volumes ($<39 \text{ \AA}^3/\text{atom}$) exhibiting octahedral lithium coordination environments (Table S1). Additionally, the more negative sulfur anion charges would lower the relative energies of LiS_4 and, hence, reduce the corresponding E_a for lithium ion migration along the *Oct–Tet–Oct* migration pathways in the *hcp*-type sulfur anion sublattices with smaller lattice volumes (Figures 3d and S16). For the sulfur anion sublattice systems with medium lattice volumes, e.g., $\sim 36.27 \text{ \AA}^3/\text{atom}$, the relative energies of LiS_4 are higher than those of LiS_6 ($E_{\text{Tet–Oct}} > 0$, Figure 3d) for the systems with the less negative sulfur anion charges ($q_s \in [-0.5e, -1.1e]$). The more negative sulfur anion charges ($q_s \in [-1.1e, -1.8e]$) make the relative energies of LiS_4 lower than those of LiS_6 ($E_{\text{Tet–Oct}} < 0$), and thereby the *Oct* sites no longer remain stable. Thereby, with the negative sulfur anion charges increasing from -0.5 to $-1.8e$, E_a first decreases and then increases (Figure S16). At larger lattice volumes, e.g., $\sim 40.16 \text{ \AA}^3/\text{atom}$, the relative energies of LiS_4 are lower than those of LiS_6 ($E_{\text{Tet–Oct}} < 0$, Figure 3d), indicating lithium prefers the *Tet* site at the large lattice volume, as shown in Table S1 for the *hcp*-type lithium sulfides with large sulfur lattice volumes ($>39 \text{ \AA}^3/\text{atom}$) showing tetrahedral lithium occupation patterns. In short, the much more negative anion charges would deliver high E_a for tetrahedral lithium ion migration along the *Tet–Oct–Tet* pathways in lithium compounds with the *hcp*-type anion sublattices but lower E_a for octahedral lithium ion migration along the *Oct–Tet–Oct* pathways.

For studying lithium ion migration in real lithium compounds with the *hcp*-type anion sublattices with respect to anion charge and lattice volume, we should first figure out the stable lithium occupation site and main lithium ion migration path. Tables S1 and S2 clearly show the lithium coordination environments in most lithium sulfides with the *hcp*-type anion sublattices are tetrahedrally coordinated, and thereby the main lithium ion migration pathways in lithium sulfides are *Tet–Tet* and *Tet–Oct–Tet*. Because E_a values of lithium ion migration along the *Tet–Tet* pathways in the *hcp*-type anion sublattices are much less sensitive to the anion charge and lattice volume than that of the *Tet–Oct–Tet* pathway, so the overall lithium ion diffusion in compounds with the *hcp* sulfur anion sublattices mainly exhibit *Tet–Oct–Tet* pathway responses to anion charge and lattice volume, and eventually the little negative anion charges would deliver low E_a for tetrahedral lithium ion migration in the *hcp*-type anion sublattices. Thus, the low negative anion charge and large lattice volume (lithium–anion bond length) are necessary for achieving fast lithium ion migration in those lithium compounds with the *hcp*-type anion sublattices and stable tetrahedral lithium occupations.

The above analyses on anion charge dependent E_a for the *hcp*-type anion sublattice model are also validated by some real lithium sulfides. Figure 4 and Table S2 show some experimentally determined and theoretically calculated E_a for tetrahedral lithium ion migration in those lithium sulfides possessing the *hcp*-type sulfur anion sublattices with respect to sulfur anion charges. As mentioned in Section 3.1 (Figure S2), lithium ion charges in different compounds do not change a lot, and thereby the anion charge variation of different lithium compounds can be regarded as resulting from the nonlithium cation element, which is fundamentally determined by the electronegativity difference between the anion element and the nonlithium cation element. In other words, the electronegativity of the nonlithium cation element M of Li–M–S

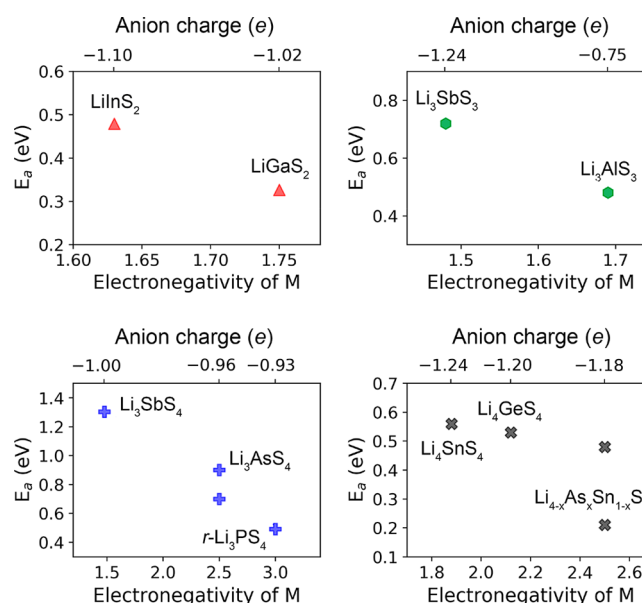


Figure 4. Experimentally determined and theoretically calculated activation energy barriers E_a of tetrahedral lithium ion migration in lithium sulfides possessing the *hcp*-type sulfur anion sublattices with respect to the electronegativity of nonlithium cation element M and sulfur anion Bader charges.^{39–45} Lithium sulfides in each subplot are structurally similar to the same space group. The corresponding data of E_a , anion charge, and electronegativity of M are also listed in Table S2.

compounds with the *hcp*-type sulfur anion sublattices can significantly affect E_a of lithium ion migration. It can be seen from Figure 4 that nonlithium cation element M has great impacts on E_a for tetrahedral lithium ion migration in those lithium sulfides with the *hcp*-type sulfur anion sublattices. For example, for the structurally similar LiMS_2 (where $M = \text{In}$ and Ga) with same space group (*Pna2*₁, No. 33), the Ga element with relatively larger electronegativity donates fewer electrons to its adjacent sulfur anions and creates a smaller average charge of the sulfur anion in LiGaS_2 than that of LiInS_2 , eventually leading to a lower E_a of tetrahedral lithium ion migration. Moreover, the same trends are also observed in Li_3MS_3 ($M = \text{Al}$ and Sb), Li_3MS_4 ($M = \text{P}$, As , and Sb), and Li_4MS_4 ($M = \text{Ge}$ and Sn). For the most lithium sulfides with the *hcp*-type sulfur anion sublattices in Table S2, there is no linear positive relationship between lattice volume and Li–S bond length (Figure S17), which is quite different from the ideal anion sublattice model. For Li_3MS_4 ($M = \text{P}$, As , and Sb) and Li_4MS_4 ($M = \text{Ge}$ and Sn), their Li–S bond lengths are found to be negatively related to the corresponding lattice volumes, and the larger Li–S bond length of Li_3PS_4 further contributes to reduced E_a together with the less negative charges of the sulfur anion. But for LiMS_2 ($M = \text{In}$ and Ga) and Li_3MS_3 ($M = \text{Al}$ and Sb), the larger Li–S bond lengths do not make the total E_a reduced as expected, while the increased E_a are due to the more negative sulfur anion charges, indicating the weight of anion charge contributing to the total E_a of those sulfides is very high. And yet there is no denying that large lattice volume (lithium–anion bond length) can lower E_a to a certain extent at any one fixed anion charge. The opposite effect of the anion charge on E_a for the *Oct–Tet–Oct* and *Oct–Oct* pathways in the *hcp*-type anion sublattices is confirmed by the experiment measured E_a and ionic conductivities of those lithium chlorides with the *hcp*-type chlorine anion sublattices

(Table S3).^{21,24} Above all, these E_a variation tendencies with respect to the substituted nonlithium cation element M validate our anion charge-lattice volume maps of the *hcp*-type anion sublattice models.

3.2. Design Strategies for Lithium Superionic Conductors. In lithium compounds, anion charges are significantly influenced by nonlithium metal elements.^{26,37} The atomic radius and valence electron configuration of the nonlithium metal element determines its coordination environment and lattice volume, eventually affecting the anion charge, lithium–anion bond length, and lithium occupation pattern. Our model analyses of the *fcc*-, *bcc*-, and *hcp*-type anion sublattices clearly demonstrate that anion charge and lattice volume (lithium–anion bond length) dramatically affect lithium ion migration especially for the *Oct–Oct* and *Oct–Oct* pathways. Therefore, it makes sense to gain low E_a for lithium ion migration by choosing the most suitable nonlithium metal element without changing the crystal structure framework a lot.

Based on the deep understandings of anion sublattice models (Figures 2, 3, and S3), two design strategies for developing new ternary ABC type lithium superionic conductors with the *fcc*-, *bcc*-, and *hcp*-type anion sublattices are proposed here: (i) for the desired lithium superionic conductors with lithium (A) ion tetrahedral occupations, the small electronegativity difference between anion elements C and nonmobile cation elements B is necessary for obtaining fast lithium (A) ion migration along the *Tet–Tet* and *Tet–Oct–Tet* pathways (Figure 5a), and the proper nonmobile cation elements B should give preference to those main group elements located at the right top of the periodic table of elements with large electronegativities, which are close to but less than that of the C elements, as shown in Figure 5b. The chemical components of the most sulfide-type superionic conductors with tetrahedral lithium ion migration along the *Tet–Tet* and *Tet–Oct–Tet* pathways, such as $\text{Li}_{10}\text{GeP}_2\text{S}_{12}$,⁹ Li_3PS_4 ,^{46,47} $\text{Li}_{1+2x}\text{Zn}_{1-x}\text{PS}_4$,¹⁶ and Li_2CuPS_4 ,⁴⁸ are completely in conformity with this tetrahedron rule; (ii) for the desired lithium superionic conductors with lithium (A) ion octahedral occupations, the large electronegativity difference between the anion elements C and the nonmobile cation elements B is essential for getting fast lithium (A) ion migration along the *Oct–Oct* and *Oct–Tet–Oct* pathways (Figure 5a), and the promising nonmobile cation elements B should give preference to those subgroup transition-metal elements located at the left bottom of the periodic table with small electronegativities, as shown in Figure 5b.

4. CONCLUSIONS

In this work, based on the density functional theory calculations and anion sublattice models, we have figured out the anion charge and lattice volume (lithium–anion bond length) dependent lithium ion diffusion in lithium compounds. The anion sublattice models clearly demonstrate that anion charge and lattice volume dramatically affect the activation energy barrier for lithium ion migration, which is validated by some reported lithium sulfides. For the tetrahedrally occupied lithium, the less negative the anion charge is, the lower the activation energy barrier is, while for the octahedrally occupied lithium, the more negative the anion charge is, the lower the activation energy barrier is. The large lattice volume (lithium–anion bond length) can lower the activation energy barrier to a certain extent. The activation energy depends more strongly on

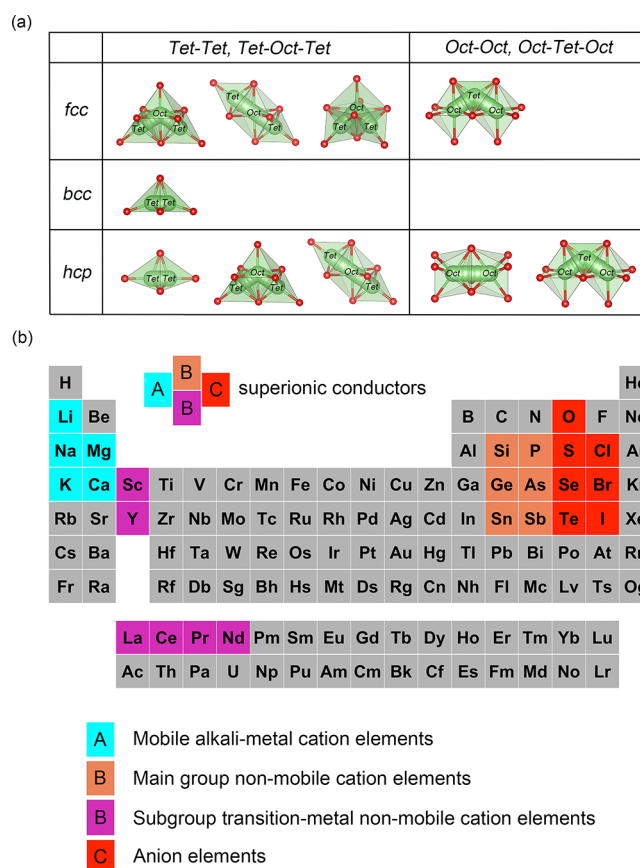


Figure 5. Design strategies for lithium superionic conductors with different lithium pathways. (a) Migration pathways of tetrahedrally and octahedrally occupied alkali-metal (A) ion in *fcc*-, *bcc*-, and *hcp*-type anion sublattices. (b) The recommended choices of nonmobile cation element B (olive and orange areas) in the periodic table of elements for achieving fast lithium (A) ion migration in the ABC ternary compounds.

lattice volume than the anion charge, while the latter could also play an important role. Lithium ion direct migrations along the direct *Tet–Tet* pathway in the *bcc*- or *hcp*-type anion sublattice are less sensitive to anion charge and lattice volume than other pathways. The much more negative anion charge and large lattice volume make lithium prefer to occupy *Tet* sites in the *hcp*-type anion sublattices, and low negative anion charge and small lattice volume make lithium preferentially occupy *Oct* sites. There are opposite effects of anion charge on the activation energy barrier and optimum lattice volumes for minimum activation energy barriers of lithium ion migration along the *Tet–Oct–Tet* and *Oct–Tet–Oct* pathways in the *hcp*-type sublattices.

Moreover, general design strategies for developing advanced lithium superionic conductors were proposed based on the full understandings of the anion sublattice model. Choosing the most suitable nonmobile cation element without changing the crystal structure framework to get the desired electronegativity difference between the anion element and the nonmobile cation element can eventually achieve a low activation energy barrier for lithium ion migration. For the desired lithium superionic conductors with lithium ion tetrahedral occupations, the small electronegativity difference between the anion element and the nonmobile cation element is necessary for obtaining fast lithium ion migration along the *Tet–Tet* and

Tet–Oct–Tet pathways, and the fine nonmobile cation elements should give preference to those elements located at the right top of the periodic table of elements with large electronegativities. For the lithium superionic conductors with lithium ion octahedral occupations, the large electronegativity difference between the anion element and the nonmobile cation element is essential for getting fast lithium ion migration along the *Oct–Oct* and *Oct–Tet–Oct* pathways, and the fine nonmobile cation elements should give preference to the elements located at the left bottom of the periodic table with small electronegativities.

■ ASSOCIATED CONTENT

SI Supporting Information

The Supporting Information is available free of charge at <https://pubs.acs.org/doi/10.1021/acs.chemmater.0c00993>.

Scatter distributions of anion Bader charge and lattice volume of lithium compounds; histogram distributions of Bader charges of lithium ion in compounds; heat maps and facetgrid plots of calculated E_a for oxygen and sulfur anion sublattices; matched *bcc* and *hcp* anion sublattices for lithium sulfides from the MP database; experimentally determined and theoretically calculated E_a of tetrahedral Li ion migration in lithium sulfides with *hcp*-type sulfur anion sublattices; scatter distributions of lattice volumes and average Li–S bond lengths of lithium sulfides with tetrahedral lithium occupations and *hcp*-type sulfur anion sublattices; E_a and $E_{\text{tet–oct}}$ matrix table data for heat maps (PDF)

■ AUTHOR INFORMATION

Corresponding Author

Hong Zhu – Shanghai Jiao Tong University, Shanghai 200240, China; orcid.org/0000-0001-7919-5661;
Email: hong.zhu@sjtu.edu.cn

Author

Zhenming Xu – Shanghai Jiao Tong University, Shanghai 200240, China; Harvard John A. Paulson School of Engineering and Applied Sciences, Harvard University, Cambridge, Massachusetts 02138, United States

Complete contact information is available at:
<https://pubs.acs.org/doi/10.1021/acs.chemmater.0c00993>

Notes

The authors declare no competing financial interest.

■ ACKNOWLEDGMENTS

This work is supported by the National Natural Science Foundation of China (51602196), Shanghai Automotive Industry Corporation (1714), and Materials Genome Initiative Center at Shanghai Jiao Tong University. Z.X. is very grateful for the fund support from the China Scholarship Council for visiting Harvard University (CSC, scholarship No. 201906230117). All calculations were performed at the Shanghai Jiao Tong University High Performance Computing Center.

■ REFERENCES

(1) Pomerantseva, E.; Bonaccorso, F.; Feng, X.; Cui, Y.; Gogotsi, Y. Energy storage: The future enabled by nanomaterials. *Science* **2019**, 366, eaan8285.

(2) Dunn, B.; Kamath, H.; Tarascon, J. M. Electrical energy storage for the grid: a battery of choices. *Science* **2011**, 334, 928–935.

(3) Harper, G.; Sommerville, R.; Kendrick, E.; Driscoll, L.; Slater, P.; Stolkin, R.; Walton, A.; Christensen, P.; Heidrich, O.; Lambert, S.; Abbott, A.; Ryder, K.; Gaines, L.; Anderson, P. Recycling lithium-ion batteries from electric vehicles. *Nature* **2019**, 575 (7781), 75–86.

(4) Zhang, Z.; Shao, Y.; Lotsch, B.; Hu, Y.-S.; Li, H.; Janek, J.; Nazar, L. F.; Nan, C.-W.; Maier, J.; Armand, M.; Chen, L. New horizons for inorganic solid state ion conductors. *Energy Environ. Sci.* **2018**, 11, 1945–1976.

(5) Judez, X.; Eshetu, G. G.; Li, C.; Rodriguez-Martinez, L. M.; Zhang, H.; Armand, M. Opportunities for Rechargeable Solid-State Batteries Based on Li-Intercalation Cathodes. *Joule* **2018**, 2, 2208–2224.

(6) Sun, C.; Liu, J.; Gong, Y.; Wilkinson, D. P.; Zhang, J. Recent advances in all-solid-state rechargeable lithium batteries. *Nano Energy* **2017**, 33, 363–386.

(7) Murugan, R.; Thangadurai, V.; Weppner, W. Fast Lithium Ion Conduction in Garnet-Type $\text{Li}_7\text{La}_3\text{Zr}_2\text{O}_{12}$. *Angew. Chem., Int. Ed.* **2007**, 46 (41), 7778–7781.

(8) Takada, K.; Tansho, M.; Yanase, I.; Inada, T.; Kajiyama, A.; Kouguchi, M.; Kondo, S.; Watanabe, M. Lithium ion conduction in $\text{LiTi}_2(\text{PO}_4)_3$. *Solid State Ionics* **2001**, 139 (3), 241–247.

(9) Kamaya, N.; Homma, K.; Yamakawa, Y.; Hirayama, M.; Kanno, R.; Yonemura, M.; Kamiyama, T.; Kato, Y.; Hama, S.; Kawamoto, K.; Mitsui, A. A lithium superionic conductor. *Nat. Mater.* **2011**, 10 (9), 682–686.

(10) Seino, Y.; Ota, T.; Takada, K.; Hayashi, A.; Tatsumisago, M. A sulphide lithium super ion conductor is superior to liquid ion conductors for use in rechargeable batteries. *Energy Environ. Sci.* **2014**, 7 (2), 627–631.

(11) Wang, Y.; Richards, W. D.; Ong, S. P.; Miara, L. J.; Kim, J. C.; Mo, Y.; Ceder, G. Design principles for solid-state lithium superionic conductors. *Nat. Mater.* **2015**, 14, 1026.

(12) He, X.; Bai, Q.; Liu, Y.; Nolan, A. M.; Ling, C.; Mo, Y. Crystal Structural Framework of Lithium Super-Ionic Conductors. *Adv. Energy Mater.* **2019**, 9 (43), 1902078.

(13) Di Stefano, D.; Miglio, A.; Robeyns, K.; Filinchuk, Y.; Lechartier, M.; Senyshyn, A.; Ishida, H.; Spannenberger, S.; Prutsch, D.; Lunghammer, S.; Rettenwander, D.; Wilkening, M.; Roling, B.; Kato, Y.; Hautier, G. Superionic Diffusion through Frustrated Energy Landscape. *Chem* **2019**, 5, 2450–2460.

(14) Blatov, V. A.; Shevchenko, A. P.; Proserpio, D. M. Applied Topological Analysis of Crystal Structures with the Program Package ToposPro. *Cryst. Growth Des.* **2014**, 14 (7), 3576–3586.

(15) Eremin, R. A.; Kabanova, N. A.; Morkhova, Y. A.; Golov, A. A.; Blatov, V. A. High-throughput search for potential potassium ion conductors: A combination of geometrical-topological and density functional theory approaches. *Solid State Ionics* **2018**, 326, 188–199.

(16) Richards, W. D.; Wang, Y.; Miara, L. J.; Kim, J. C.; Ceder, G. Design of $\text{Li}_{1+2x}\text{Zn}_{1-x}\text{PS}_4$, a new lithium ion conductor. *Energy Environ. Sci.* **2016**, 9 (10), 3272–3278.

(17) Kato, Y.; Hori, S.; Saito, T.; Suzuki, K.; Hirayama, M.; Mitsui, A.; Yonemura, M.; Iba, H.; Kanno, R. High-power all-solid-state batteries using sulfide superionic conductors. *Nature Energy* **2016**, 1 (4), 16030.

(18) Fisher, C. A. J.; Hart Prieto, V. M.; Islam, M. S. Lithium Battery Materials LiMPO_4 (M = Mn, Fe, Co, and Ni): Insights into Defect Association, Transport Mechanisms, and Doping Behavior. *Chem. Mater.* **2008**, 20 (18), 5907–5915.

(19) Gardiner, G. R.; Islam, M. S. Anti-Site Defects and Ion Migration in the $\text{LiFe}_{0.5}\text{Mn}_{0.5}\text{PO}_4$ Mixed-Metal Cathode Material. *Chem. Mater.* **2010**, 22 (3), 1242–1248.

(20) Wang, S.; Bai, Q.; Nolan, A. M.; Liu, Y.; Gong, S.; Sun, Q.; Mo, Y. Lithium Chlorides and Bromides as Promising Solid-State Chemistries for Fast Ion Conductors with Good Electrochemical Stability. *Angew. Chem., Int. Ed.* **2019**, 58 (24), 8039–8043.

(21) Asano, T.; Sakai, A.; Ouchi, S.; Sakaida, M.; Miyazaki, A.; Hasegawa, S. Solid Halide Electrolytes with High Lithium-Ion

Conductivity for Application in 4 V Class Bulk-Type All-Solid-State Batteries. *Adv. Mater.* **2018**, *30*, 1803075.

(22) Krauskopf, T.; Muy, S.; Culver, S. P.; Ohno, S.; Delaire, O.; Shao-Horn, Y.; Zeier, W. G. Comparing the Descriptors for Investigating the Influence of Lattice Dynamics on Ionic Transport Using the Superionic Conductor $\text{Na}_3\text{PS}_{4-x}\text{Se}_x$. *J. Am. Chem. Soc.* **2018**, *140* (43), 14464–14473.

(23) Kraft, M. A.; Ohno, S.; Zinkevich, T.; Koerver, R.; Culver, S. P.; Fuchs, T.; Senyshyn, A.; Indris, S.; Morgan, B. J.; Zeier, W. G. Inducing High Ionic Conductivity in the Lithium Superionic Argyrodites $\text{Li}_{6+x}\text{P}_{1-x}\text{Ge}_x\text{S}_5\text{I}$ for All-Solid-State Batteries. *J. Am. Chem. Soc.* **2018**, *140* (47), 16330–16339.

(24) Muy, S.; Voss, J.; Schlem, R.; Koerver, R.; Sedlmaier, S. J.; Maglia, F.; Lamp, P.; Zeier, W. G.; Shao-Horn, Y. High-Throughput Screening of Solid-State Li-Ion Conductors Using Lattice-Dynamics Descriptors. *iScience* **2019**, *16*, 270–282.

(25) Kraft, M. A.; Culver, S. P.; Calderon, M.; Bocher, F.; Krauskopf, T.; Senyshyn, A.; Dietrich, C.; Zevalkink, A.; Janek, J.; Zeier, W. G. Influence of Lattice Polarizability on the Ionic Conductivity in the Lithium Superionic Argyrodites $\text{Li}_6\text{PS}_5\text{X}$ ($\text{X} = \text{Cl}, \text{Br}, \text{I}$). *J. Am. Chem. Soc.* **2017**, *139* (31), 10909–10918.

(26) Xu, Z. M.; Bo, S. H.; Zhu, H. LiCrS_2 and LiMnS_2 Cathodes with Extraordinary Mixed Electron-Ion Conductivities and Favorable Interfacial Compatibilities with Sulfide Electrolyte. *ACS Appl. Mater. Interfaces* **2018**, *10*, 36941–36953.

(27) Xu, Z.; Chen, X.; Liu, K.; Chen, R.; Zeng, X.; Zhu, H. Influence of Anion Charge on Li Ion Diffusion in a New Solid-State Electrolyte, Li_3LaI_6 . *Chem. Mater.* **2019**, *31* (18), 7425–7433.

(28) Xu, Z.; Chen, X.; Chen, R.; Li, X.; Zhu, H. Anion charge and lattice volume dependent lithium ion migration in compounds with *fcc* anion sublattices. *npj Computational Materials* **2020**, *6*, 47.

(29) Blöchl, P. E. Projector augmented-wave method. *Phys. Rev. B: Condens. Matter Mater. Phys.* **1994**, *50* (24), 17953–17979.

(30) Verma, P.; Truhlar, D. G. Status and Challenges of Density Functional Theory. *Trends in Chemistry* **2020**, *2* (4), 302–318.

(31) Perdew, J. P.; Burke, K.; Ernzerhof, M. Generalized Gradient Approximation Made Simple. *Phys. Rev. Lett.* **1996**, *77* (18), 3865–3868.

(32) Kohn, W.; Sham, L. J. Self-Consistent Equations Including Exchange and Correlation Effects. *Phys. Rev.* **1965**, *140* (4A), A1133–A1138.

(33) Monkhorst, H. J.; Pack, J. D. Special points for Brillouin-zone integrations. *Phys. Rev. B* **1976**, *13* (12), 5188–5192.

(34) Henkelman, G.; Jónsson, H. Improved tangent estimate in the nudged elastic band method for finding minimum energy paths and saddle points. *J. Chem. Phys.* **2000**, *113* (22), 9978–9985.

(35) Curtarolo, S.; Setyawan, W.; Hart, G. L. W.; Jahnatek, M.; Chepulskii, R. V.; Taylor, R. H.; Wang, S.; Xue, J.; Yang, K.; Levy, O.; Mehl, M. J.; Stokes, H. T.; Demchenko, D. O.; Morgan, D. AFLOW: An automatic framework for high-throughput materials discovery. *Comput. Mater. Sci.* **2012**, *58*, 218–226.

(36) Li, K.; Xue, D. Estimation of electronegativity values of elements in different valence states. *J. Phys. Chem. A* **2006**, *110* (39), 11332–7.

(37) Krauskopf, T.; Culver, S. P.; Zeier, W. G. Bottleneck of Diffusion and Inductive Effects in $\text{Li}_{10}\text{Ge}_{1-x}\text{Sn}_x\text{P}_2\text{S}_{12}$. *Chem. Mater.* **2018**, *30* (5), 1791–1798.

(38) Culver, S. P.; Koerver, R.; Krauskopf, T.; Zeier, W. G. Designing Ionic Conductors: The Interplay between Structural Phenomena and Interfaces in Thiophosphate-Based Solid-State Batteries. *Chem. Mater.* **2018**, *30* (13), 4179–4192.

(39) Murayama, M.; Sonoyama, N.; Yamada, A.; Kanno, R. Material design of new lithium ionic conductor, thio-LISICON, in the $\text{Li}_2\text{S}-\text{P}_2\text{S}_5$ system. *Solid State Ionics* **2004**, *170* (3–4), 173–180.

(40) Sahu, G.; Lin, Z.; Li, J.; Liu, Z.; Dudney, N.; Liang, C. Air-stable, high-conduction solid electrolytes of arsenic-substituted Li_4SnS_4 . *Energy Environ. Sci.* **2014**, *7* (3), 1053–1058.

(41) Kanno, R. Synthesis of a new lithium ionic conductor, thio-LISICON–lithium germanium sulfide system. *Solid State Ionics* **2000**, *130* (1–2), 97–104.

(42) Rao, F.-Y.; Ning, F.-H.; Jiang, L.-W.; Zeng, X.-M.; Wu, M.-S.; Xu, B.; Ouyang, C.-Y. First principle study of LiXS_2 ($\text{X} = \text{Ga}, \text{In}$) as cathode materials for Li ion batteries. *Chin. Phys. B* **2016**, *25* (2), 028202.

(43) Gamon, J.; Duff, B. B.; Dyer, M. S.; Collins, C.; Daniels, L. M.; Surta, T. W.; Sharp, P. M.; Gaultois, M. W.; Blanc, F.; Claridge, J. B.; Rosseinsky, M. J. Computationally Guided Discovery of the Sulfide Li_3AlS_3 in the Li–Al–S Phase Field: Structure and Lithium Conductivity. *Chem. Mater.* **2019**, *31* (23), 9699–9714.

(44) Al-Qawasmeh, A.; Holzwarth, N. A. W. Computational Study of Li Ion Electrolytes Composed of Li_3AsS_4 Alloyed with Li_4GeS_4 . *J. Electrochem. Soc.* **2016**, *163* (9), A2079–A2088.

(45) Kwak, H.; Park, K. H.; Han, D.; Nam, K.-W.; Kim, H.; Jung, Y. S. Li^+ conduction in air-stable Sb-Substituted Li_4SnS_4 for all-solid-state Li-Ion batteries. *J. Power Sources* **2020**, *446*, 227338.

(46) Tachez, M.; Malugani, J.-P.; Mercier, R.; Robert, G. Ionic conductivity of and phase transition in lithium thiophosphate Li_3PS_4 . *Solid State Ionics* **1984**, *14* (3), 181–185.

(47) Homma, K.; Yonemura, M.; Kobayashi, T.; Nagao, M.; Hirayama, M.; Kanno, R. Crystal structure and phase transitions of the lithium ionic conductor Li_3PS_4 . *Solid State Ionics* **2011**, *182* (1), 53–58.

(48) Xu, Z.; Chen, R.; Zhu, H. A Li_2CuPS_4 superionic conductor: a new sulfide-based solid-state electrolyte. *J. Mater. Chem. A* **2019**, *7* (20), 12645–12653.